Calcite as polar biomineral with a tendency for glass formation

Yang Yang [1,*] Yixin Lin,[1] Boyuan Gou,[1] Xiangdong Ding,[1,†] Jun Sun,[1] Christopher J. Howard [2] and Ekhard K. H. Salje[3,‡]
[1]State Key Laboratory for Mechanical Behaviour of Materials, Xi'an Jiaotong University, Xi'an 710049, China
[2]School of Engineering, The University of Newcastle, University Drive, Callaghan, New South Wales 2308, Australia
[3]Department of Earth Sciences, University of Cambridge, Cambridge CB2 3EQ, United Kingdom

(Received 21 May 2025; revised 17 August 2025; accepted 23 September 2025; published 14 October 2025)

Calcite, $CaCO_3$, is a widely available biomaterial with remarkable properties. Its twin walls (TWs), formed during growth or deformation, show intriguing properties including a strong polarization. While calcite has no macroscopic dipole moment (by symmetry) the TWs show a big shift in the distance between Ca^{2+} and CO_3^{2-} resulting in dipole moments (polarization) estimated at 0.22 C/m^2. Such strong dipole moments have a substantial influence on the diffusion of atoms inside twin boundaries. Furthermore, deformation will also generate simple kinks inside the TWs. These kinks lead to local clusters of amorphized $CaCO_3$. Stressed calcite, in devices or in the natural environment, will be riddled with such kinks, which explains the tendency to form locally amorphized materials. The structural particularities of calcite originate from a sequence of phase transitions, thermal or by growth, from a cubic phase to a rhombohedral phase with $R\bar{3}m$ symmetry to the $R\bar{3}c$ phase known at room temperature. Symmetry aspects of these transitions are discussed. The complexity of the TW structure arises from both the odd-even effect at the twin boundary in the rhombohedral structure and the coupling between two order parameters in the phase transitions of calcite. The coupling scheme is linear quadratic and is discussed in detail.

DOI: 10.1103/mpmg-71ck

I. INTRODUCTION

As the most stable polymorph of calcium carbonate ($CaCO_3$), calcite plays a critical role in planetary formation and function. It occurs widely in primitive solar system chondrites [1], including the parent body of the recently visited asteroid Bennu [2], and is a recurrent phase of supracrustal rocks on Mars [3]. On Earth it is the principal constituent of sedimentary limestone, by far the largest repository of atmospheric CO_2 over deep time [4,5]. For the past 500 million years or so most of this production has been co-opted by carbonate-biomineralizing organisms, tapping into both its ready availability and its unique material properties.

Calcite is a relatively brittle, soft, trigonal mineral with high birefringence, perfect cleavage, and a pronounced tendency to form twins. Despite its familiarity to classical mineralogists, geologists, and (paleo-)biologists, there has been surprisingly little consideration of its atomic-scale structure, particularly at twin boundaries where Ca^{2+} and the CO_3^{2-} triangles are necessarily realigned to accommodate the intersecting geometries. Its structural, mechanical, and electrical properties are closely related to its two main phase transitions [6,7]. The high-temperature phase is calculated to be cubic with $Fm\bar{3}m$ symmetry [8]. Cooling calcite reduces the symmetry first to $R\bar{3}m$ and finally to the $R\bar{3}c$ room temperature structure. These transitions greatly modify the physical and chemical properties of calcite by injecting strong micro- and nanotwinning [9–11].

Chemically, the twin planes are expected to show exceptionally high rates of diffusion and reactivity and they provide key insights into the ordering and modification of the underlying atomic-scale architecture [12,13]. Twin planes are likely to be sites of enhanced CO_2 loss, potentially at levels high enough to compete with bulk diffusion. First-principles calculations suggest that preferential adsorption along twin walls (TWs) alter the mechanical stability of calcite [14]. High chemical reactivity is also known to occur at the intersection between twin boundaries and crystal surfaces [14]. Twinning occurs commonly in natural "biocalcite," where both growth twins [15,16] and nanoscale deformation twins [17] have been adopted for the toughening and/or hardening of biomineralized structures well beyond the limits of mineralogical "geocalcite" [4,5,18]. These TWs appear to play a key role in modifying the properties of calcite for its roles in skeletons [19] and other biological situations [17]. Different types of twins (*e*, *f*, and *r* twins) crosscutting each other are often found in the same grain [20]. Among these twins, the *r*-type $104 = \{10\bar{1}4\}_{hex}$ twin is considered to play an important role in the deformation of calcite [21]. Significantly, our recent molecular dynamics modeling identified a number of unexpected features associated with the {104} TW, including an inherently bilayer structure, kinks showing high structural disorder, and an exceptionally strong dipole moment [22]. Ultimately, we expect twin planes to emerge as a first-order control over the biological transformation of amorphous calcium carbonate (ACC) to calcite via the aggregation and collective integration of the constituent nanoparticles [23–25].

The predominant role of twin boundaries relates to the displacements of cations and anions inside the TWs that lead to a rearrangement of charges. While the bulk is

*Contact author: yangymse@xjtu.edu.cn
†Contact author: dingxd@mail.xjtu.edu.cn
‡Deceased.

electrically neutral, twin boundaries exhibit strong internal dipole moments that are known from previous studies of other materials to be the basis for generating electronic devices like transistors and photovoltaic devices, as well as for local superconductivity and enhanced conductivity [26–34]. In this paper, we describe the temperature dependence of the wall polarization and more generally, derive suitable Landau potentials for the two phase transitions of calcite [35]. We show that the main ingredient is the coupling of the order parameters of the two phase transitions. This coupling has unusual symmetry properties: it is linear in one order parameter and quadratic in the other. This linear-quadratic coupling was predicted theoretically [8,36–38] and we quantify the coupling mechanism in this paper. We then show that the coupling is also crucial to understanding the structure of the active twin boundaries [39–41]. Here, the most important parameter is the strong electrostatic polarization of the twin boundaries, which was systematically observed in twinned materials [42–44]. The strong electrostatic interactions were already identified in calcite for the formation of glassy and amorphous phases. It was also identified for the role of water and/or protein molecules [45]. Yang *et al*. [22] have shown that kink formations in the bulk lead to glassy beads inside calcite near the kink position [46–48]. We confirm and extend these observations. Our work was greatly stimulated by recent electron microscopical observations by Németh [49] and computer simulations by Bruno *et al*. [50].

II. METHODS

A. Molecular dynamics simulations

The phase transformation behavior and TW profiles were studied by molecular dynamics (MD) simulations based on an empirical potential of $CaCO_3$ generated by Raiteri *et al.* [51]. The parameters were fitted against experimental thermodynamic and structural data [22]. Previous studies have shown that this potential can provide a good description of the $\{10\bar{1}4\}_{hex}$ TW structure and the phase transitions of $CaCO_3$ over a wide temperature range, from 20 to 2000 K [8,22]. It is important to note that these simulations implicitly assume CO_2 partial pressures sufficiently elevated to avoid the decomposition of $CaCO_3$ even at temperatures exceeding calcite's decomposition temperature of approximately 1100 K at ambient pressure.

In this paper we focused on the TW polarity and linear-quadratic order parameter coupling in calcite at different temperatures. Therefore, we first built two different three-dimensional models with two base ions or ion groups (Ca^{2+}, CO_3^{2-}) carrying opposite charges of +2 and −2, respectively. Consequently, variations in partial atomic charges due to structural changes or local atomic environments are neglected. The first model contained two parallel TWs and had dimensions of $32.2 \times 36.3 \times 4.0$ nm^3 (384 000 atoms). A pristine sample with the same dimension and orientation was used as a reference to study the order parameter coupling effects in the bulk. Periodic boundary conditions were applied along the x, y, and z; directions for both models there is thus no free surface in our simulations.

Structural relaxations were calculated under a fixed number of particles, pressure, and temperature (*NPT* ensemble [52]) for 0.5 ns with a time step of 1 fs. The temperature and pressure were controlled by a Nosé-Hoover thermo- and barostat [52–54]. The MD simulations were performed with the LAMMPS code [55] and the atomic patterns are displayed via the open visualization tool, OVITO [56,57].

B. Definition of order parameters

The high-temperature phase of $CaCO_3$ is cubic with $Fm\bar{3}m$ symmetry [8]. Cooling calcite reduces the symmetry first to $R\bar{3}m$ and finally to the $R\bar{3}c$ room temperature structure. The thermodynamic analysis of these transitions [8] indicates that in each case the order parameter has only one independent component, thus it is effectively scalar. The $Fm\bar{3}m \rightarrow R\bar{3}m$ transition is a ferroelastic phase transformation, involving a structural change from a cubic to a rhombohedral lattice. Beyond the alteration in lattice symmetry, the most significant change in this transition is the transformation of the CO_3^{2-} ion symmetry from a spherical distribution to a planar (ring-shaped) distribution. The $R\bar{3}m \rightarrow R\bar{3}c$ transition is primarily driven by an orientational order-disorder transition of the CO_3^{2-} ions. Crucially, the orientational ordering of CO_3^{2-} in the $R\bar{3}c$ phase results in a doubling of the unit-cell volume.

We define two order parameters in calcite to describe these structural evolutions. The first describes the $Fm\bar{3}m$-$R\bar{3}m$ transition and is denoted Q_Γ, since the order parameter relates to the Γ point within the Brillouin zone of the $Fm\bar{3}m$ space group. This transition is necessarily stepwise, unless a singular point is encountered [58] due to a third-order term in thermodyamic potential [59], and is proper ferroelastic. The transition from the $R\bar{3}m$ phase to $R\bar{3}c$ is not ferroelastic and is symmetry allowed to be continuous. The relevant order parameter [8] relates to the T point of the $R\bar{3}m$ Brillouin zone (or to the L point of the cubic Brillouin zone) and is here denoted Q_T.

As mentioned above, the most obvious characteristic of the $Fm\bar{3}m$-$R\bar{3}m$ transition is the symmetry of the distribution of the CO_3^{2-} molecules, which transforms from random (spherical) to planar under cooling. The order parameter Q_Γ will thus be well represented as a quantity that describes the out-of-plane tilting angle θ of CO_3^{2-} groups. It is estimated from

$$Q_\Gamma = \frac{1}{N}\sum\left\langle 1 - \frac{\theta_i}{\theta_{av}}\right\rangle, \tag{1}$$

where θ_i represents the tilt angle (in degrees) of the ith CO_3^{2-} group in the system under study, θ_{av} is the mean value of the tilting angle of spherically distributed (i.e., randomly oriented) CO_3^{2-} anions, the symbol $\langle\cdot\rangle$ means a time average, and N means the total number of $CaCO_3$ groups in the system. We can easily obtain the value of θ_{av}, which is equal to 57.3° (1 radian), through polar coordinate integration (see Supplemental Material Note I [60]). In the $Fm\bar{3}m$ phase, where the CO_3^{2-} ions exhibit a spherical distribution, the value of Q_Γ is zero; in the $R\bar{3}m$ phase, where the CO_3^{2-} ions adopt a planar distribution (all θ_i are zero), Q_Γ takes a value of 1. The order parameter Q_Γ as defined in Eq. (1) is normally positive; in the study of twinning, however, it is useful to see a sign change across a twin boundary (see Figs. 10 and 11) so we leave Q_Γ

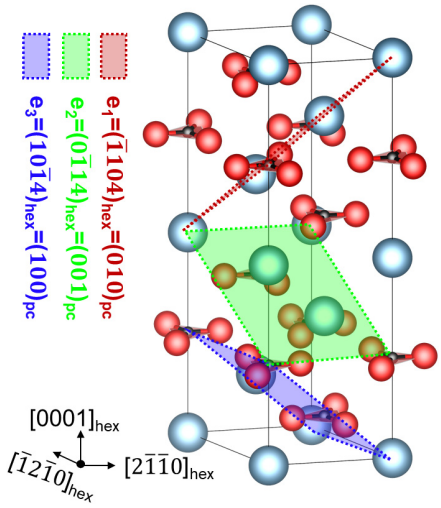

FIG. 1. Hexagonal structural cell of $CaCO_3$. The red, green, and blue planes are equivalent lattice planes for calcite; they are {001} lattice planes in a pseudocubic structural cell.

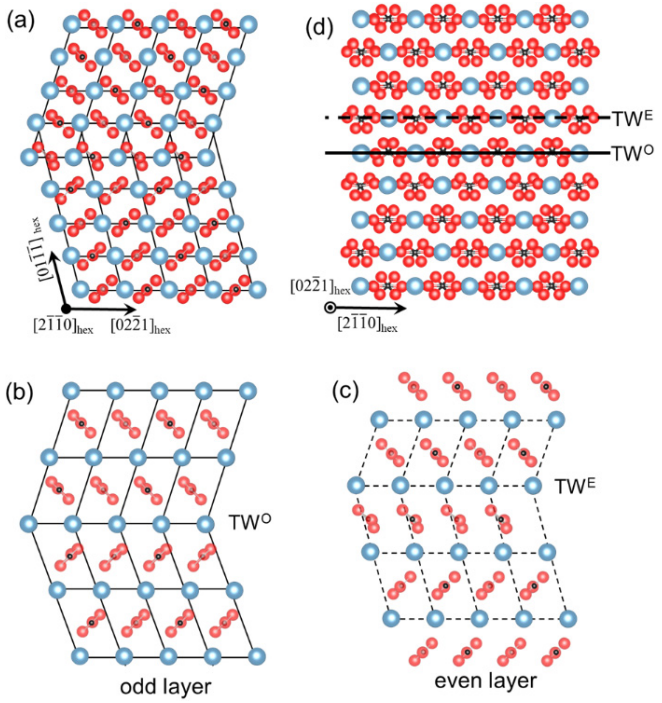

FIG. 2. Schematic structure of (a) the TW, here taken to be on $(0\bar{1}14)_{hex}$. The structure consists of two layers of $CaCO_3$ molecules. The views are along $[2\bar{1}\bar{1}0]_{hex}$ so they are projections onto the $(2\bar{1}\bar{1}0)_{hex}$ plane. These layers are named "even" and "odd" in (b) and (c). The TW is the superposition of the two types of layers. (d) Each subwall is either TW^O or TW^E; their superposition leads to strong structural strains in (a).

positive in one twin domain but attach a negative sign in an adjacent twin domain.

Q_T describes the phase transition of the $R\bar{3}m$-$R\bar{3}c$. At low temperatures in the $R\bar{3}c$ phase, the CO_3^{2-} groups are ordered in layers with opposite orientations in adjacent $(0001)_{hex}$ layers (Supplemental Material Fig. S1 [60]). In the higher-temperature $R\bar{3}m$ phase, this orientational ordering of CO_3^{2-} triangles is lost, for example, if the parallel and antiparallel orientations occur at random. We thus estimate Q_T, as in our previous work [22], by the in-plane rotations of CO_3^{2-} triangles:

$$Q_T\langle(-1)^L\cos(3\varphi_i)\rangle, \tag{2}$$

where φ_i is the angle between the a axis of the crystal (hexagonal cell) and a randomly chosen carbon-oxygen (C-O) bond of the ith CO_3^{2-} ion. L enumerates the layers. In the $R\bar{3}m$ phase, the CO_3^{2-} groups exhibit a disordered arrangement, yielding $Q_T = 0$; in the $R\bar{3}c$ phase, the CO_3^{2-} groups adopt an ordered configuration, resulting in $Q_T = 1$. The value of Q_T remains invariant under different twin orientations; consequently, we do not employ sign distinctions to differentiate between twin variants for Q_T.

For the calculation of both order parameters, we have adopted a combined temporal-spatial averaging approach to ensure enhanced accuracy in our computations. For ergodic systems, temporal averaging is equivalent to spatial averaging, both being identical to ensemble averaging. The equivalence of spatial and temporal averaging has been rigorously verified in the Supplemental Material [60] (as shown in Supplemental Material Fig. S2).

III. RESULTS AND DISCUSSION

A. The structure of $\{10\bar{1}4\}_{hex}$ twin walls

We focus on one particular TW, the r type, which is dominant in calcite, although other TWs may also be important. This twinning occurs across the $\{10\bar{1}4\}_{hex}$ planes (Fig. 1), which coincide with the main cleavage planes $\{001\}_{pc}$ in the equivalent pseudocubic setting [11]. Shown in Fig. 2 are different projections of the calcite crystal structure, which is taken to be twinned across $(0\bar{1}14)_{hex}$: the views in (a), (b), and (c) are along $[2\bar{1}\bar{1}0]_{hex}$ and therefore onto $(2\bar{1}\bar{1}0)_{hex}$ planes, and the view in (d) is along $[20\bar{2}\bar{1}]_{hex}$. The $(2\bar{1}\bar{1}0)_{hex}$ planes constitute layers that are distinguished in (b) and (c) as odd and even; the offset between these layers is a consequence of the rhombohedral crystal structure. In addition, the CO_3^{2-} groups in calcite in the low-temperature form ($R\bar{3}c$ phase) are ordered in such a way that CO_3^{2-} groups inside the same $(0001)_{hex}$ plane are parallel (i.e., have the same orientation), but are alternately antiparallel and parallel in subsequent layers. As the TWs intersect these layers, it leads to rather complex crystal structures of the boundaries. This means that a TW cannot be one-atom-layer thin; the minimum thickness is two layers with strain fields increasing this minimum thickness (Fig. 2).

The crucial topological feature is that the TWs in calcite cannot be thin, with minimum thickness two layers (≈ 0.6 nm). This is fundamentally different from twin boundaries in prototypical ferroelastics such as $Pb_3(PO_4)^2$ [37,40,61], where the strain-induced wall thickness is ten unit cells [39]. In $CaTiO_3$ the observed wall thickness is ~0.4 nm [27], where the thickness as seen in TEM is ca. two octahedra similar to the results of MD simulations [41]. Typically, the thickness of a TW can be estimated by the strain changes on both sides of the interface. The evolution of shear strain in the

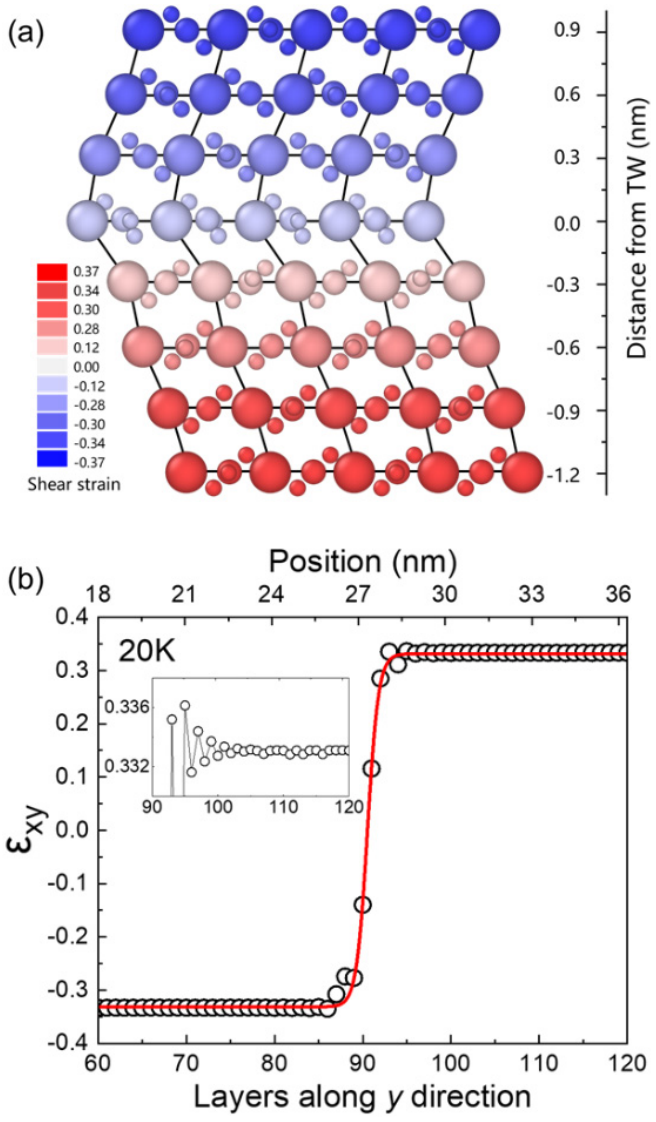

FIG. 3. (a) Shear strain near a TW. (b) Fitting the shear strain by a classic tanh $\frac{x}{w}$ profile. The inset figure in (b) shows the oscillations of the shear strain caused by distortions near the TW [63].

TW can be fitted by a classic tanh $\frac{x}{w}$ profile [62]. Figure 3(a) shows the evolution of shear strain near a TW at 20 K. To highlight the subtle differences in shear strain across different atomic layers, we applied a nonlinear coloring scheme to the strain. It shows that even at a distance of ∼1.0 nm from the TW, the shear strain still differs from that in the bulk (±0.33 at 20 K). The fitted TW width w is 0.412 nm [Fig. 3(b)].

The relatively low values of our estimated TW thicknesses are due to the fact that the tanh formula does not accurately describe the behavior of twin boundaries, such as the oscillations in shear strain caused by distortions near the boundary [inset in Fig. 3(b)]. Another important reason is that the shear strain is calculated by using the positions of the Ca^{2+} ions, while the distortion of CO_3^{2-} ions in TWs is also significant.

The strong structural distortions in TWs lead to shifts between cations and anions (Fig. 4). This implies that the twin boundaries display strong dipole moments [28,41,42]. Figure 4(a) illustrates the dipole structure within eight atomic layers near the TW. Polar displacement is the displacement of the positive Ca^{2+} from the center of the six neighboring negative CO_3^{2-} ions. The green arrows indicate this displacement, which is caused by large lattice distortions near the TW. On the left side of Fig. 4(a), the magnitude of the mismatch between the positive and negative charge centers in different atomic layers is shown.

The polarization near the TW is not limited to the eight atomic layers adjacent to the wall. Figure 4(b) shows the variation in the displacement of positive and negative charge centers and polarization as a function of distance (in terms of atomic layers) from the TW at different temperatures. The polarization is $P = \frac{qs}{V}$, where q is the ionic charge, s is the polar displacement in each formula unit, and V is the volume of the formula unit, taken to be one-sixth of the volume of the unit cell (367.85 $Å^3$). The polar displacement spans approximately 20 atomic layers or 6 nm.

The great thickness of TWs in $CaCO_3$ is primarily due to the odd-even effect inherent in its structure. Figures 4(c) and 4(d) respectively illustrate the dipole moments in odd and even layers. At the twin boundary the dipole moments in the odd and even layers are similarly aligned. It can be seen, however, that within each of these layers the dipole directions reverse, more or less, between one twin variant and the other; furthermore, these directions are reversed (aside from at the boundary itself) between odd and even layers. The dipole moments gradually decay to zero with increasing distance from the TW. Another significant reason for the increased thickness of the TW lies in the coupling between two distinct order parameters in the structure (Q_T and Q_Γ), which will be further discussed in the following sections.

As the temperature increases, the dipole moment near the TW weakens due to thermal vibrations reducing the lattice distortions near the interface. Figure 5 illustrates the temperature dependence of polarization density at TWs. We analyzed the average polarization density over TW regions of varying thickness. For example, Fig. 5 shows the average polarization density of the two atomic layers closest to the TW center, which reaches 0.2 C/m² at 20 K. When the TW region thickens, the polarization density decreases (See Supplemental Material Fig. S3 [60]). This reduction can be attributed to two factors: first, the diminished lattice distortion with increasing distance from the TW, leading to weaker polarization, and second, the mutual cancellation of opposing dipoles in adjacent layers.

Kinks are common within twin boundaries and are considered as "walls within walls" [64–66]. The presence of kinks makes the movement of two-dimensional interfaces much easier [65]. We have shown the atomic structure of a kink inside the $\{10\bar{1}4\}_{hex}$ TW [22]. Significant distortions and glassy regions are observed near kinks. This is very different from kinks in other materials, where kinks are very localized and interact with each other but do not form glass states.

The structural destabilization induced by kink formation suggests that an increased kink density may expand the affected region, potentially transforming the entire twin boundary into a glassy phase. As demonstrated in Fig. 6, several closely spaced kinks [Fig. 6(a)] can cooperatively generate an extended amorphous interface structure. Upon structural relaxation at room temperature, internal stresses

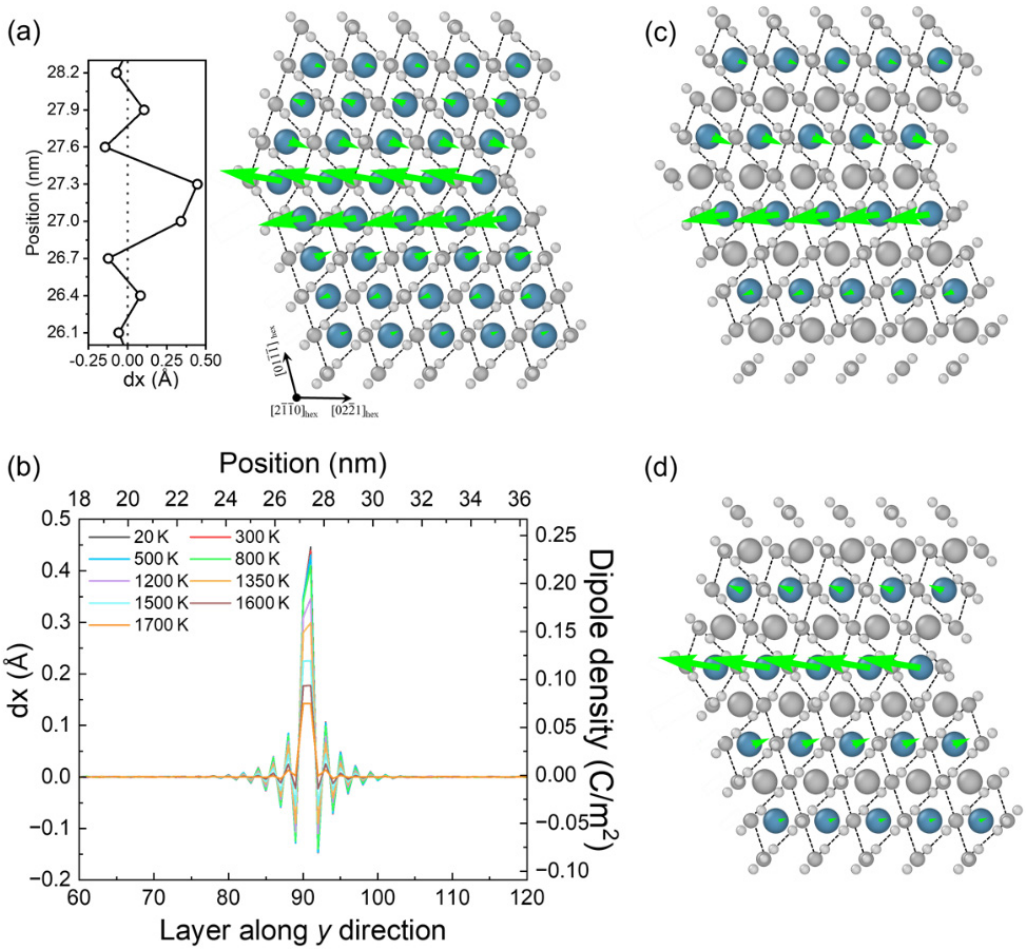

FIG. 4. Dipole moments in TWs of $CaCO_3$. (a) Lattice distortion near TWs induces displacement of positive and negative charge centers. Green arrows indicate the displacements of Ca^{2+} with respect to the center of charge of the six surrounding CO_3^{2-} groups. (b) Displacement or dipole density evolution as functions of distance from TWs at 20, 300, 500, 800, 1200, 1350, 1500, 1600, and 1700 K. (c) and (d) highlight odd and even layers, respectively (atoms in blue), along with the associated Ca^{2+} displacements.

arising from this high density of kinks induce severe lattice distortion and subsequent amorphization [Figs. 6(b)–6(d)]. This transformation occurs rapidly, completing within 1.5 ps.

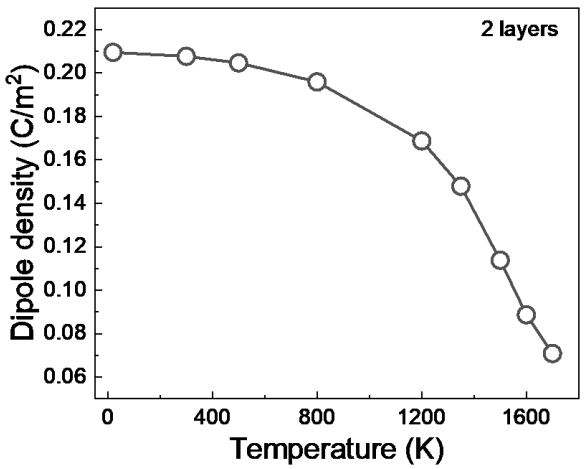

FIG. 5. Temperature evolution of dipole moments in TWs of calcite.

Concurrently, the significant volume fraction of the amorphous phase results in measurable volumetric expansion, as evident in Fig. 6(d). Following prolonged structural relaxation (100 ps), a portion of the amorphous domains reverts to a crystalline state, reducing the overall amorphous volume fraction [Fig. 6(e)]. Nevertheless, persistent amorphous domains remain localized at the TWs [Fig. 6(f)]. This mechanism provides insight into the natural behavior of stressed calcite in both engineered devices and geological environments where a high kink density can explain the material's propensity for localized amorphization.

Radial distribution function (RDF) analysis was employed to confirm the presence of a kink-induced amorphous phase at the interface. Figure 7 presents the evolution of Ca-Ca, Ca-C, Ca-O, C-C, C-Ca, and C-O RDFs within the amorphous interfacial region (red curves) and the pristine crystalline bulk (black curves). The bulk region exhibits characteristic features of a perfect crystal structure, manifested by multiple sharp, well-defined peaks in the RDF profiles. Owing to the inherent symmetry of the crystal lattice, the Ca-Ca RDF in the bulk is identical to the C-C RDF, while the Ca-C and C-Ca RDFs are also indistinguishable. These distinctive signatures provide conclusive evidence of the crystalline state in the

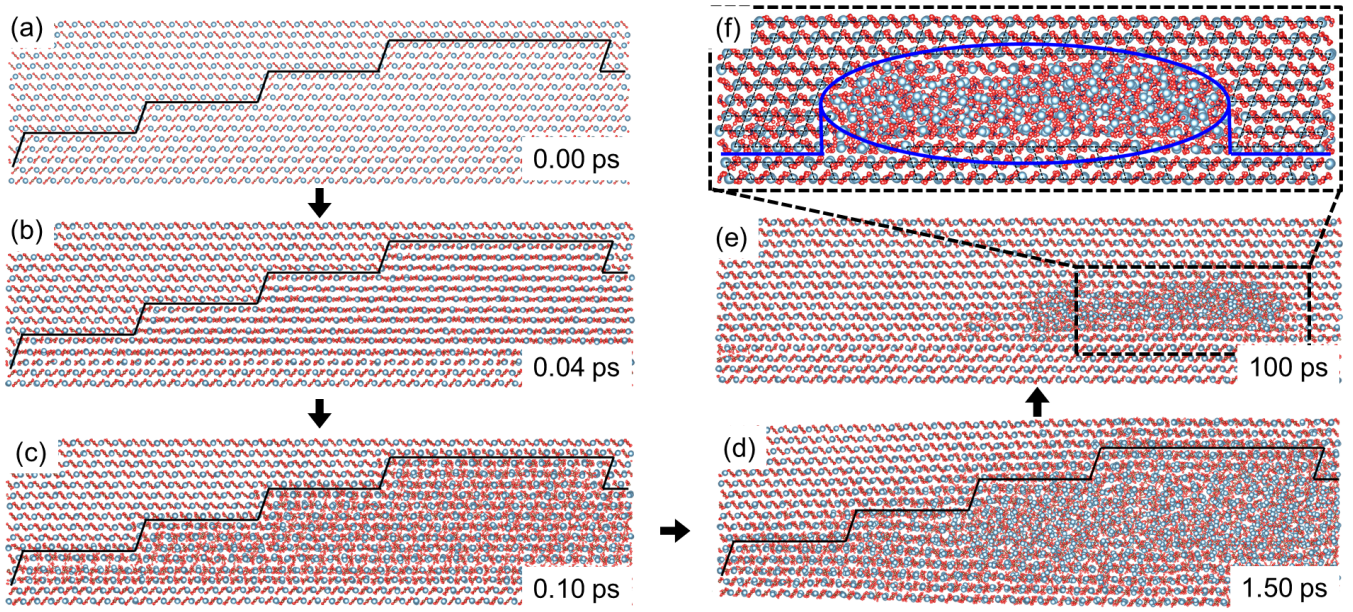

FIG. 6. Extended amorphous interface structure generated by three closely spaced kinks. (a) Original atomic arrangement of three closely spaced kinks. (b)–(d) Rapid amorphization induced by internal stresses arising from high density of kinks. (e) Stable amorphous region after a long structure relaxation. (f) Detailed structures of amorphous region in TWs.

bulk region. In stark contrast, the kink-induced amorphous interface displays no sharp peaks. Instead, broad, featureless humps dominate the RDF profiles—a hallmark characteristic of amorphous structures. It is noteworthy that within the C-O RDF of the amorphous region, the first coordination peak persists, signifying the preservation of covalent bonding between carbon and oxygen atoms.

Notably, these amorphous domains (ACC) exhibit strong affinity for dopant accumulation and impurity segregation [67,68]. There are a number of reasons for this: (1) The inherently disordered structure of ACC facilitates the incorporation of dopants and impurities into its matrix [69]. (2) Incorporated impurities can impede the crystallization process (transformation of ACC to calcite), thereby enhancing the stability

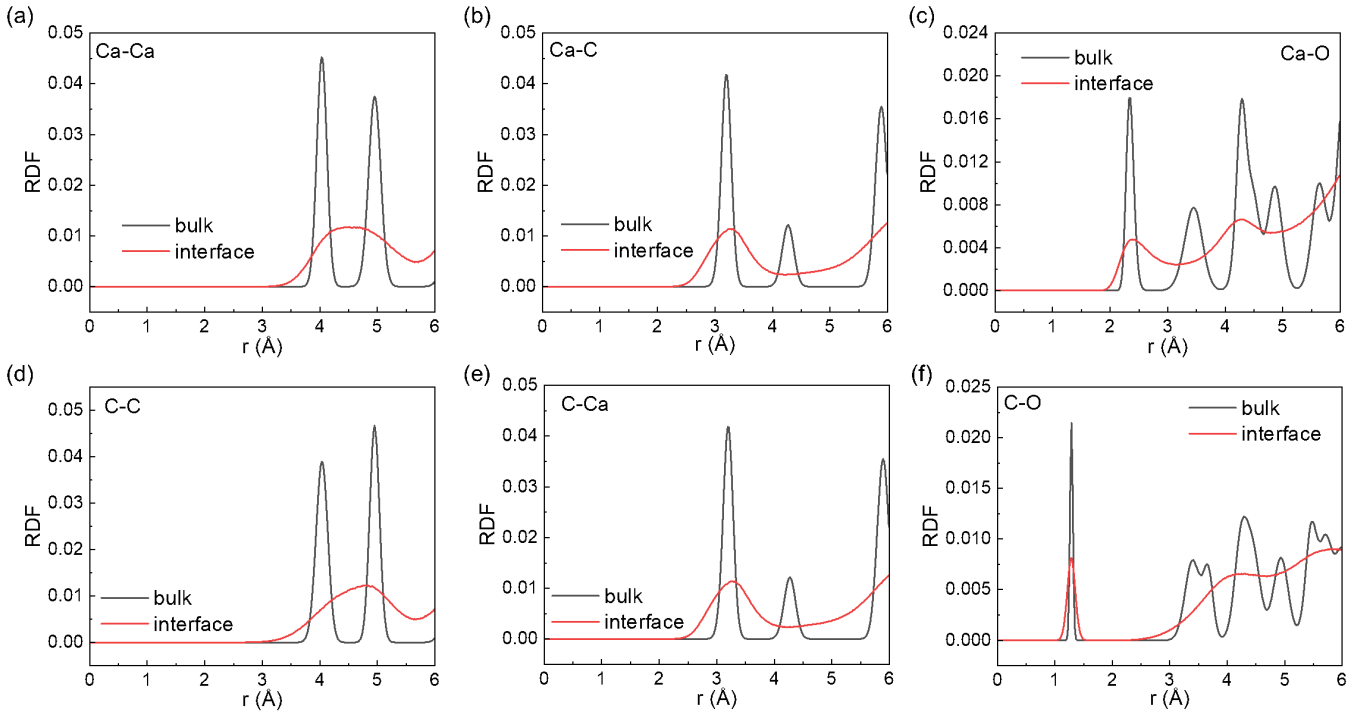

FIG. 7. Comparison of the (a) Ca-Ca, (b) Ca-C, (c) Ca-O, (d) C-C, (e) C-Ca, and (f) C-O radial distribution functions within the amorphous interfacial region (red curves) with those in the pristine crystalline bulk (black curves).

of the ACC phase [70]. (3) The large specific surface area and high reactivity of ACC domains provide abundant sites for the adsorption of dopants and impurities [69]. Furthermore, we quantified the polarization within the ACC domains depicted in Fig. 6(e). The measured polarization intensity reaches 1.09 $\mathrm{C\,m^{-2}}$, approximately fivefold greater than that observed in conventional TWs. This significantly enhanced polarization serves as compelling evidence for the heightened dopant adsorption capacity of ACC regions. The observed amorphization pathway, mediated by kink-density modulation at twin boundaries, represents a previously unreported material transformation mechanism in crystalline systems. This discovery challenges the conventional understanding of deformation-induced amorphization processes and suggests new possibilities for interface engineering through defect density control.

B. Bulk coupling of order parameters

Structural instabilities are not independent but interact giving rise to several coupling phenomena [71]. The "faintness" of coupling is determined by symmetry wherein the faintness parameter is the exponent of the order parameter in the coupling term in the Gibbs free energy of the phase transitions [72]. The Gibbs free energy is now cast into a Landau potential with the following symmetry-allowed terms [8,35,72–74]:

$$G_\Gamma = \frac{1}{2}C\Theta_s^\Gamma\left[\coth\left(\frac{\Theta_s^\Gamma}{T}\right)-\coth\left(\frac{\Theta_s^\Gamma}{T_\Gamma}\right)\right]Q_\Gamma^2+\frac{1}{3}bQ_\Gamma^3+\frac{1}{4}Q_\Gamma^4, \tag{3}$$

$$G_\mathrm{T} = \frac{1}{2}A\Theta_s^\mathrm{T}\left[\coth\left(\frac{\Theta_s^\mathrm{T}}{T}\right)-\coth\left(\frac{\Theta_s^\mathrm{T}}{T_\mathrm{T}}\right)\right]Q_\mathrm{T}^2+\frac{1}{4}Q_\mathrm{T}^4, \tag{4}$$

where A, b, and C are normalized parameters in the Landau potential. T_Γ and T_T refer to the transition temperatures for the $Fm\bar{3}m$-$R\bar{3}m$ and $R\bar{3}m$-$R\bar{3}c$ transitions, respectively. Θ_S^Γ and $\Theta_\mathrm{S}^\mathrm{T}$ are characteristic temperatures [73] for these two transitions, respectively. The term in (3) of third degree drives the transition $Fm\bar{3}m$-$R\bar{3}m$ to be stepwise whereas all previously considered transitions were continuous.

The total Gibbs free energy G is the sum of these two expressions of G_Γ and G_T plus the term that describes the interaction between the two order parameters. This "coupling term" is symmetry constrained. The lowest-order symmetry-allowed coupling term is [8]

$$G_\mathrm{coupling} = L\left(Q_\mathrm{T}^2Q_\Gamma^1\right) = \tfrac{1}{2}\lambda Q_\mathrm{T}^2Q_\Gamma. \tag{5}$$

Hence the faintness index is 1 for Q_Γ and 2 for Q_T and the coupling is linear quadratic [75]. The stable solution is determined by the equilibrium conditions

$$\frac{\partial G}{\partial Q_\Gamma}=0 \quad \text{and} \quad \frac{\partial G}{\partial Q_\mathrm{T}}=0. \tag{6}$$

The resulting equations can be solved by a simple shift of the order parameter Q_Γ to Q_Γ^*.

$$Q_\Gamma^* = Q_\Gamma + \frac{b}{3}, \tag{7}$$

which simplifies Eq. (6) to a simple third-order polynomial

$$Q_\Gamma^{*\,3} + \left(c^* - \tfrac{1}{2}\lambda^2\right)Q_\Gamma^* - \tfrac{1}{2}\lambda a^* = 0, \tag{8}$$

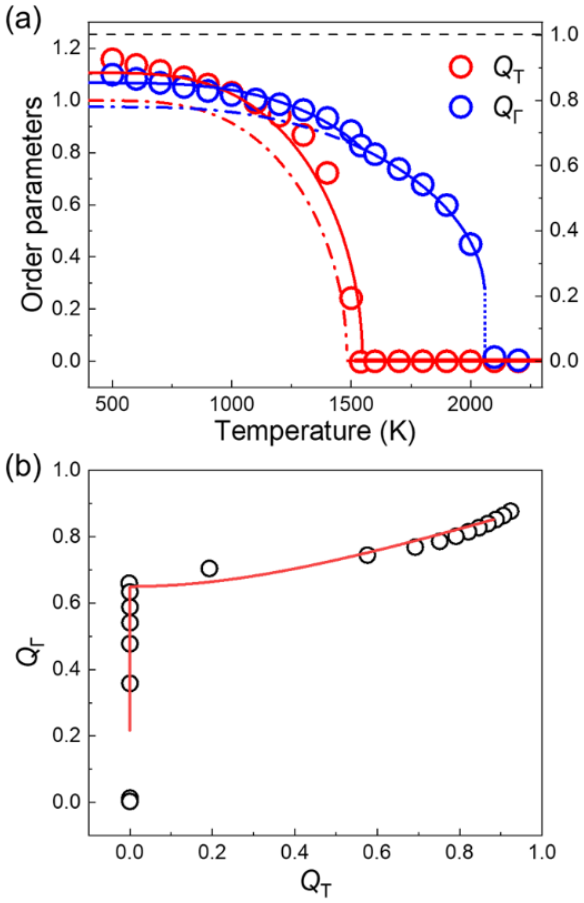

FIG. 8. Evolution of order parameters under heating induces structural phase transformations in calcite. (a) Temperature evolution of the two order parameters in calcite. The red curve represents the in-plane order parameter Q_T with a projected transition temperature near 1550 K. The out-of-plane tilt described by Q_Γ (blue curve) is not yet saturated at this temperature but jumps here by approximately 20%. The dot-dashed lines show the bare, i.e., uncoupled, order parameters. (b) Order parameter vector space of the two order parameters Q_Γ and Q_T. The black circles show the results of MD simulations [22] and the red line is the result of the Landau potential described in this paper.

which contains no quadratic term in Q_Γ^* or Q_T with renormalized a^* and c^*.

The equations in G_Γ^* and G_T are now used to calculate the two order parameters. The relevant closed-form equations are listed in Supplemental Material Note II [60].

Figure 8(a) shows the temperature evolution of the two order parameters. All the circles result from MD simulations. By fitting these MD data, we can obtain all the coefficients and the coupling constant λ in the above equations. The bold lines show the equilibrium evolutions of the order parameters. The dot-dashed lines show the two order parameters without coupling. The stepwise transition in Q_Γ is indicated by a dotted line. The most obvious characteristic feature of the coupling is the hump in the Q_Γ curve near the transition temperature T_T. This proves that the tilt (out-of-plane) movement of the CO_3^{2-} groups is far from saturated below the transition point of Q_T. When the in-plane ordering increases it also increases the

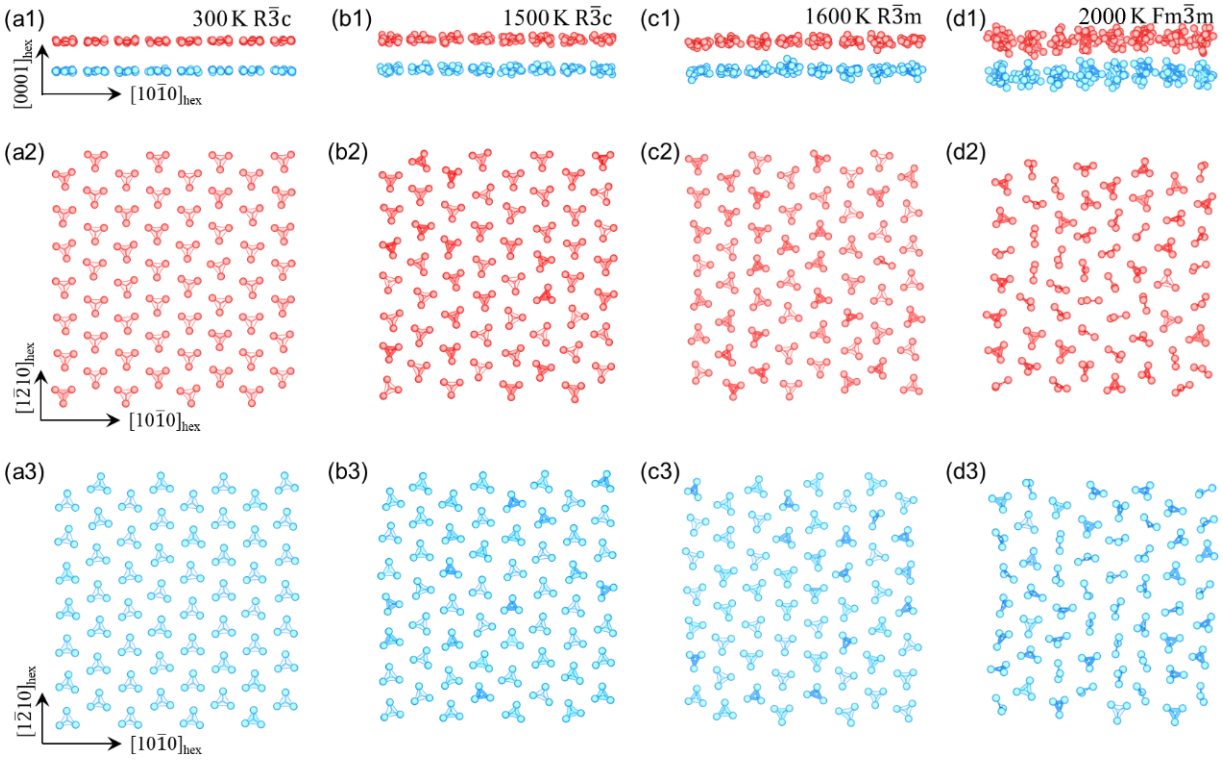

FIG. 9. Typical orientations of CO_3^{2-} groups in two adjacent $(0001)_{hex}$ atomic layers at (a) 300 K, (b) 1500 K, (c) 1600 K, and (d) 2000 K. Red and blue represent the odd and even layers, respectively.

tilt ordering. For purposes of presentation, theoretical results without coupling are referenced to the axis on the left, whereas both theoretical with coupling and the MD results are shown against the axis on the right. The coupling between the order parameters above T_T can be neglected. The order parameter vector space of the two order parameters Q_T and Q_Γ is shown in Fig. 8(b).

Figure 9 shows typical orientations of two adjacent $(0001)_{hex}$ CO_3^{2-} layers at temperatures of 300, 1500, 1600, and 2000 K. At 300 and 1500 K, calcite exists in the $R\bar{3}c$ phase, where the orientation of CO_3^{2-} is relatively strong. Specifically, within each plane, the orientations of all triangular units are nearly identical, as indicated in Figs. 9(a) and 9(b). The out-of-plane tilting is rather weak. When the structure transitions to the $R\bar{3}m$ phase, in-plane orientations of the triangular units lose the parallel-antiparallel ordering scheme of the room temperature phase, signaling the disappearance of the order parameter Q_T (Fig. 8). The out-of-plane tilting is stronger than in the $R\bar{3}c$ phase, but the CO_3^{2-} entity itself remains planar. As the temperature increases further, so does the out-of-plane tilting. As the temperature rises further, transitioning calcite to the cubic $Fm\bar{3}m$ phase, both order parameters vanish, corresponding to fully random in-plane and out-of-plane orientations throughout the system [Fig. 9(d)].

MD simulations revealed critical temperatures for the $R\bar{3}c$ to $R\bar{3}m$ and $R\bar{3}m$ to $Fm\bar{3}m$ transitions are 1525 and 1900 K, respectively [8], While the decomposition temperature of calcite at ambient pressure is only ∼1100 K. However, our MD simulations systematically overestimate phase transition temperatures compared to experimental data. For instance, while the experimental $R\bar{3}c$ to $R\bar{3}m$ transition occurs near 1240 K [76], our simulation yields a value of ∼1525 K, representing an overestimation of approximately 23%. Extrapolating this error margin suggests the experimental transition temperature for the subsequent $R\bar{3}m$ to $Fm\bar{3}m$ phase transition could be reduced from 1900 K to approximately 1540 K. Critically, at this lower extrapolated temperature, it may be feasible to suppress calcite decomposition by elevating CO_2 partial pressure, thereby enabling experimental observation of this previously unreported phase transition.

C. Coupling in twin walls

The same order parameter coupling as in the bulk is now described for TWs [77]. Yang *et al*. already determined that emerging properties exist in calcite because TWs are polar while the bulk is not [22]. The idea that such properties exist is relatively new and has not been employed for calcite [4,5,11,16,18,78]. "Exotic" interfaces were previously found in WO_3 (superconducting walls [79]), $BiFeO_3$ and $LiNbO_3$ (conducting walls [80,81]), $SrTiO_3$, and $CaTiO_3$ (polar walls [27,29,82,83]). The unusual coupling mechanism in calcite TWs relates to the linear-quadratic coupling between the order parameters, which seems extremely rare in other materials [84,85]. In contrast, biquadratic coupling is always symmetry allowed and very common [36,86,87], similarly local flexoelectric coupling leading to so-called ripple states [88]. The case of linear-quadratic coupling was first analyzed theoretically as a new type of interaction by Salje and Carpenter [75]. Pöttker and Salje explored the consequences of such coupling more widely for interfacial properties where one order parameter forms a twin boundary and the second reacts

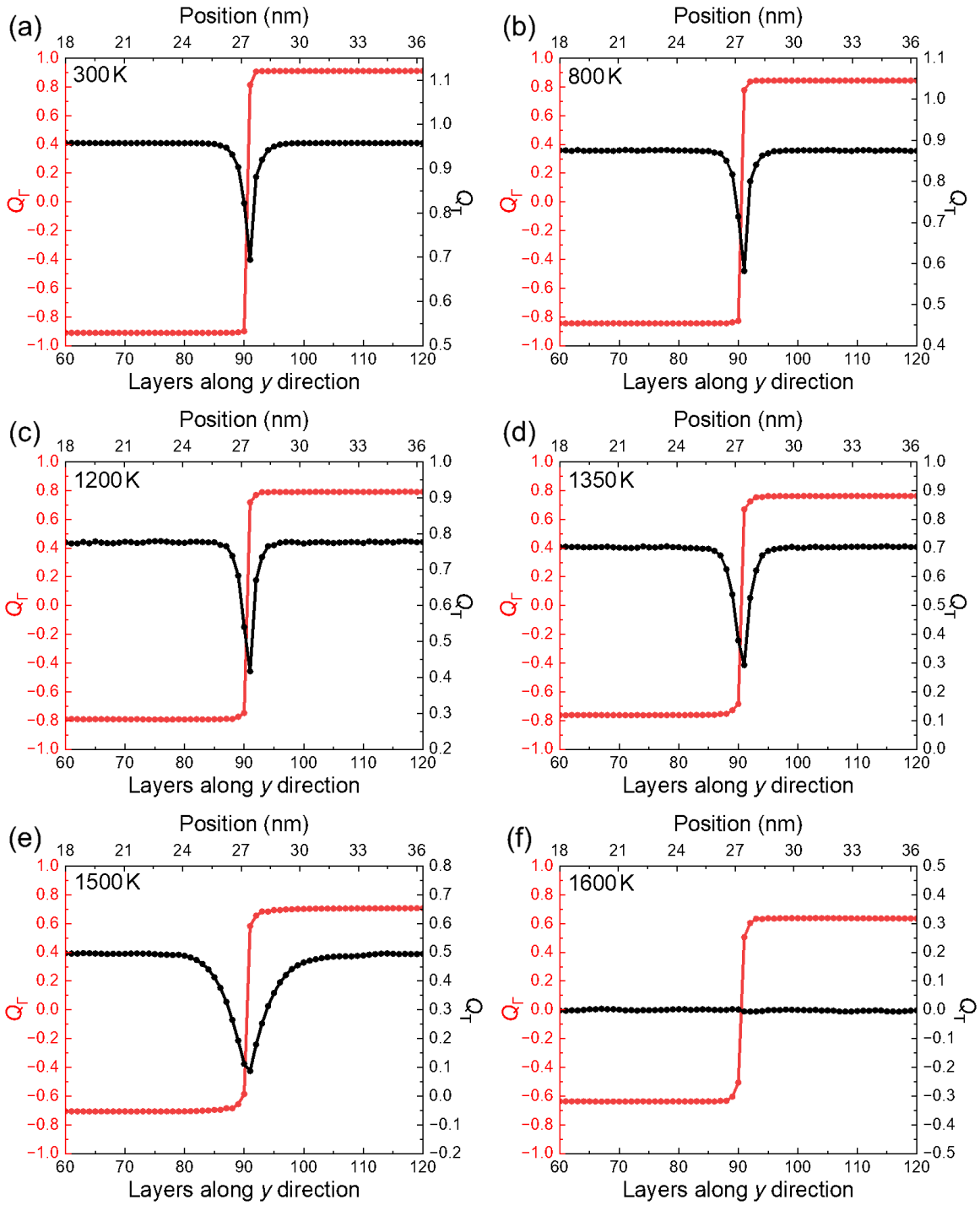

FIG. 10. Wall profiles in linear-quadratic coupling at (a) 300 K, (b) 800 K, (c) 1200 K, (d) 1350 K, (e) 1500 K, and (d) 1600 K. For all temperatures, Q_Γ follows a tanh profile while Q_T superimposes a cusp profile.

to these boundary conditions [88]. No concrete experimental examples were found previously. We summarize the theoretical predictions as follows:

(1) If only one order parameter contributes to the wall profile, the profiles follow the classic tanh function very well.

(2) If two order parameters contribute to the wall profile, the solutions are kinks and breathers, where one order parameter changes sign and the other decreases from its equilibrium value only within the domain wall.

(3) If the relative strength of the leading-order gradient terms reaches a critical value, the interface is divided into two separate transitions. The closer the order parameters pass the point (0,0), the weaker the coupling.

Based on the theoretical topological solutions of two coupling order parameters in TWs, we checked the twin wall profile of calcite by MD simulations. The topological solutions are calculated using the interaction parameters derived by Yang *et al.* [22]. Figure 10 shows the evolution of the

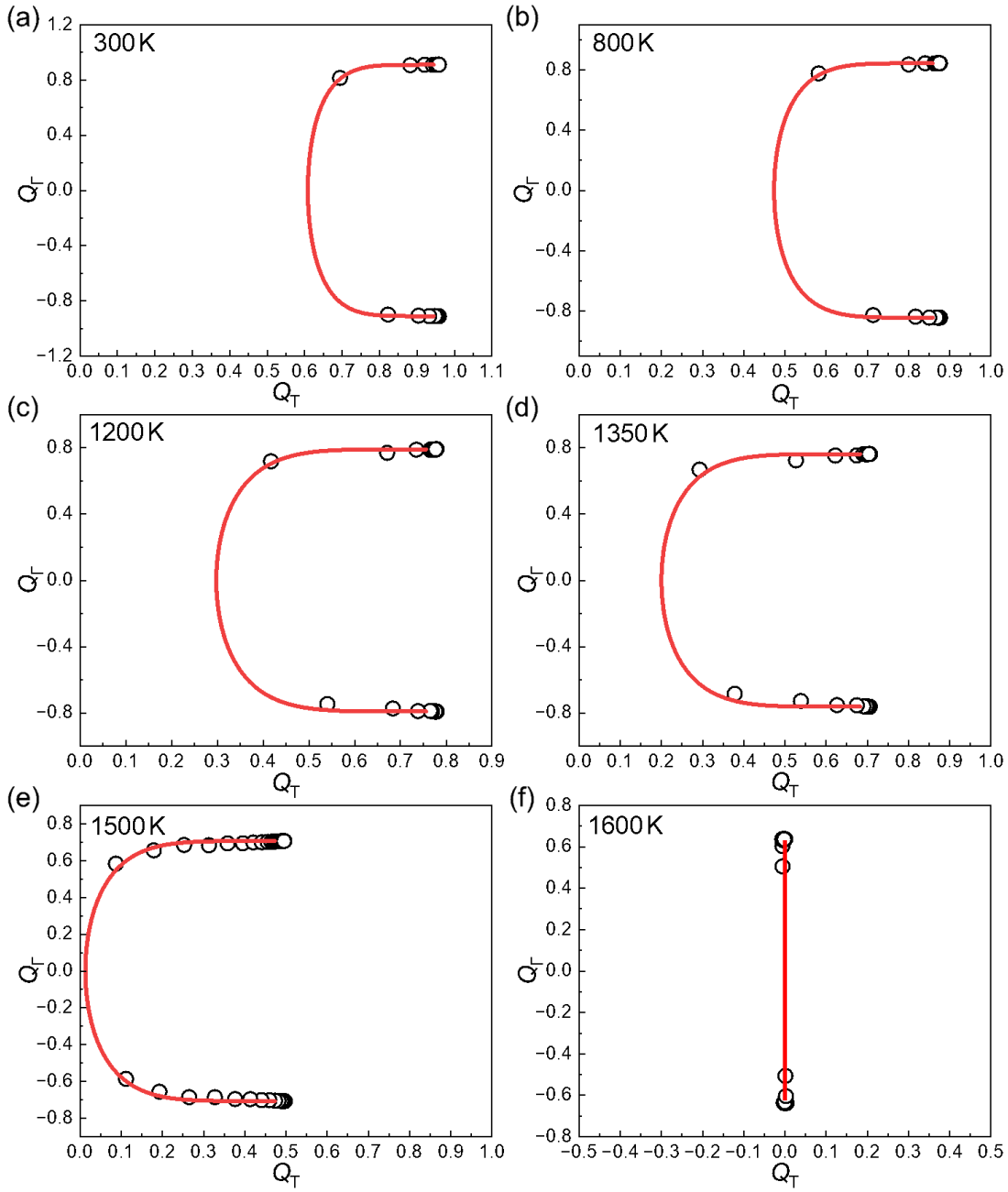

FIG. 11. Order parameter vector spaces for TWs at (a) 300 K, (b) 800 K, (c) 1200 K, (d) 1350 K, (e) 1500 K, and (f) 1600 K.

two order parameters, i.e., Q_T and Q_Γ near $\{10\bar{1}4\}_{hex}$ TWs at temperatures of 300, 800, 1200, 1350, 1500, and 1600 K. The calcite is in $R\bar{3}c$ phase at temperatures below 1523 K, and in $R\bar{3}m$ phase at 1600 K. There are no TWs in the $Fm\bar{3}m$ phase.

For all temperatures we find that Q_Γ follows an approximately tanh profile while Q_T superimposes a breatherlike profile. The "breather" of Q_T represents the influence range of TWs, or in other words, the thickness of TWs. It is evident that in the $R\bar{3}c$ phase, the TW thickness increases with rising temperature. After transitioning to the $R\bar{3}m$ phase, the coupling between Q_T and Q_Γ vanished entirely.

We describe the Q_T profile as "breatherlike" because a true breather exhibits a much broader minimum in its spatial distribution, whereas the minima observed in Figs. 10(a)–10(e) are relatively sharp. For this reason, we designate such sharp minima as "cusps." The reason for the cusp minimum in Q_T lies in the highly complex domain-wall configurations in calcite, which are inherently linked to the odd-even effect in TWs. This phenomenon generates abrupt discontinuities in orientational order parameters at the twin boundaries, as the odd-even effect imposes competing constraints on the in-plane rotations of CO_3^{2-} groups. The existing theoretical frameworks fail to adequately describe the evolution of the Q_T profile because it deviates from a conventional breather behavior. Figure 11 shows the order parameter vector space for the TWs. Figure 11(f) confirms the absence of order parameter coupling in the $R\bar{3}m$ phase.

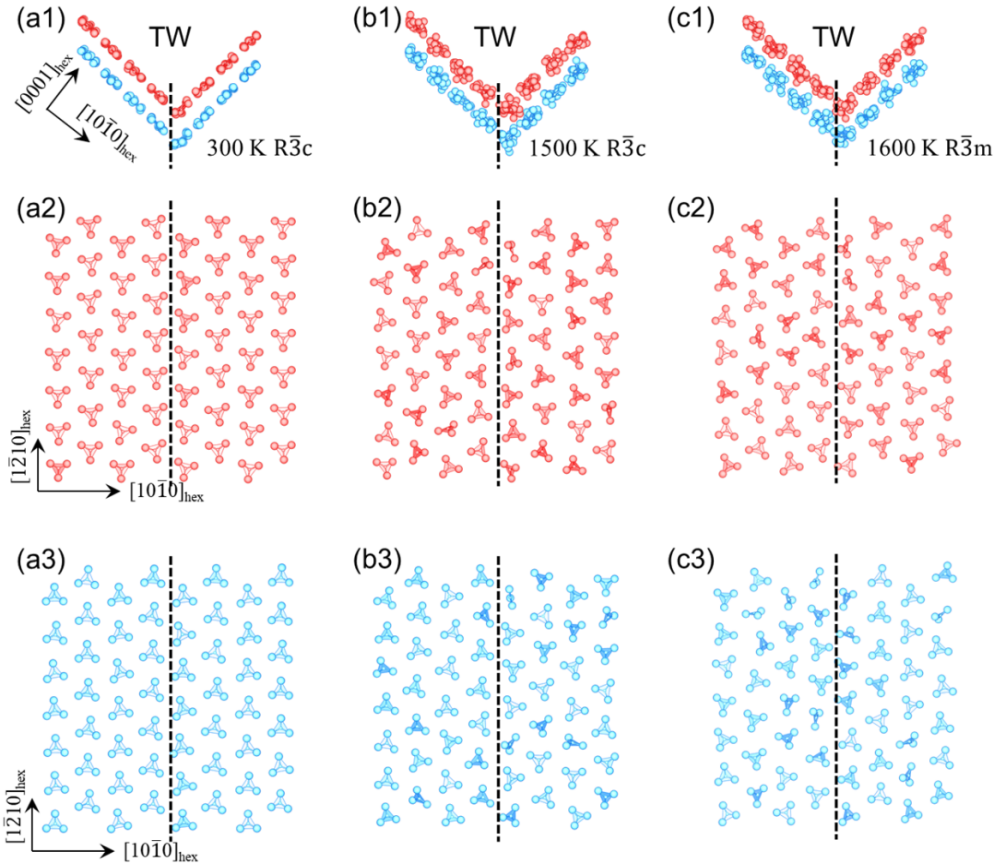

FIG. 12. Typical orientations of CO_3^{2-} groups in two adjacent $(0001)_{hex}$ atomic layers near a TW at (a) 300 K, (b) 1500 K, and (c) 1600 K. Red and blue represent the odd and even layers, respectively.

Figures 12(a)–12(c) illustrate the orientational characteristics of the CO_3^{2-} groups at the TW at 300, 1500, and 1600 K. Compared with the orientations observed in the bulk (Fig. 9), the CO_3^{2-} groups at the TW exhibit the following distinctive features:

(1) *Enhanced out-of-plane tilting*. At the same temperature, the out-of-plane tilting is more pronounced at the TW [Figs. 12(a)–12(c)], corresponding to a reduction in Q_Γ at the TW.

(2) *Increased in-plane disorder.* A direct comparison between Figs. 12 and 9 reveals significantly intensified in-plane rotational dynamics of CO_3^{2-} groups near the TW compared to the bulk. While residual in-plane correlations persist [Figs. 12(a) and 12(b)], the orientational mismatch between neighboring triangular units becomes more pronounced at the TW, leading to a marked decrease in Q_T.

(3) *Nonzero Q_T with spatial decay in $R\bar{3}c$ phase*. Despite the reduced Q_T at the TW, it remains nonzero in the $R\bar{3}c$ phase, indicating incomplete loss of in-plane correlations among CO_3^{2-} groups. Notably, the magnitudes of both in-plane rotation and out-of-plane tilting progressively diminish with increasing distance from the TW, highlighting the localized nature of these orientational perturbations.

IV. CONCLUSIONS

Calcite is not only one of the most available biomaterials on Earth, it is also one of the oldest minerals. It was found in samples of the asteroid (101955) Bennu returned by the OSIRIS-Rex mission in 2024 [2]. In engineering applications, calcite is already used as binder in the construction of platforms for landing strips in the South China sea and its mechanical use has been explored in much detail by the Ortiz group at Massachusetts Institute of Technology [17,19]. One of the key ingredients for its mechanical stability is the fact that twinned calcite is hard; twinning arises because stressed calcite reduces stress by the formation of TWs. We have shown that these TWs, specifically the {104} TWs, have a more complex crystal structure compared with TWs in other materials such as perovskites [27,71,89]. The complexity of the TWs in calcite stems from the offset of successive layers inherent in its rhombohedral structure [as shown in Figs. 2(b) and 2(c)] at ambient temperatures. Upon cooling, calcite undergoes a progressive reduction of its symmetry from cubic $Fm\bar{3}m$ to rhombohedral $R\bar{3}m$ to rhombohedral $R\bar{3}c$. This symmetry reduction is due to two interacting phase transitions, which we discussed in this paper. The dominant emerging property of TWs is the polarization and it is expected that this polarity is transmitted to the surface of calcite (steps). It will then strongly interact with dopants and adsorbents such as water, iron, and amino acids.

The interaction between the relevant order parameters is linear quadratic in its energy term. This bulk interaction is mirrored by the TWs where energies of the type $Q_T Q_\Gamma^2$ generate TWs that have a typical tanh profile in Q_Γ while Q_T follows a cusp profile at the same locus. Polarity disappears in the cubic

phase where twins are symmetry forbidden. The "exotic" wall profiles also lead to another peculiar feature of TWs. When TWs are subjected to even very weak stress, they form kinks [90]. While kinks in most other materials are very localized and interact with each other, kinks in calcite destabilize the structure and form locally glassy structures. In cases with high kink concentrations, entire twin walls can become local phases with glass features that will attract dopants as impurities [21]. The extent of such glass formation of twin walls has not been seen in other materials. It is possible that the locus of such combined clustering is inside the twin boundaries [91], which are ubiquitous in Precambrian fossils. This aspect will be researched in the future.

ACKNOWLEDGMENTS

Y.Y. and X.D. are grateful for the financial support by the National Natural Science Foundation of China (Grants No. 12104355 and No. W2411048), Sustainable Support Project Funding, the China Postdoctoral Science Foundation (Grant No. 2022M722508), Key Technologies R&D Program (Grant No. 2022YFB3707601), the Fundamental Research Funds for the Central Universities (Grant No. xzy012023168), and the 111 project 2.0 (BP2018008). E.K.H.S. is grateful to EPSRC for support under grant No. EP/P024904/1.

DATA AVAILABILITY

The data that support the findings of this article are not publicly available upon publication because it is not technically feasible and/or the cost of preparing, depositing, and hosting the data would be prohibitive within the terms of this research project. The data are available from the authors upon reasonable request.

[1] S. de Leuw, A. E. Rubin, and J. T. Wasson, Carbonates in CM chondrites: Complex formational histories and comparison to carbonates in CI chondrites, Meteorit. Planet. Sci. **45**, 513 (2010).

[2] T. J. McCoy *et al.*, An evaporite sequence from ancient brine recorded in Bennu samples, Nature (London) **637**, 1072 (2025).

[3] P. B. Niles, D. C. Catling, G. Berger, E. Chassefière, B. L. Ehlmann, J. R. Michalski, R. Morris, S. W. Ruff, and B. Sutter, Geochemistry of carbonates on Mars: Implications for climate history and nature of aqueous environments, Space Sci. Rev. **174**, 301 (2013).

[4] C. Castillo Alvarez, J. L. Grimsich, C. A. Schmidt, H. Lisabeth, A. Voigtländer, and P. U. P. A. Gilbert, Calcite twinning in mollusk shells and Carrara marble, Adv. Funct. Mater. **34**, 2304288 (2023).

[5] N. Floquet and D. Vielzeuf, Mesoscale twinning and crystallographic registers in biominerals, Am. Mineral. **96**, 1228 (2011).

[6] L. Bayarjargal, C. J. Fruhner, N. Schrodt, and B. Winkler, $CaCO_3$ phase diagram studied with Raman spectroscopy at pressures up to 50 GPa and high temperatures and DFT modeling, Phys. Earth Planet. Inter. **281**, 31 (2018).

[7] E. Salje and K. Viswanathan, The phase diagram calcite-aragonite as derived from the crystallographic properties, Contrib. Mineral. Petrol. **55**, 55 (1976).

[8] Y. Yang, Y. Lin, X. Ding, C. J. Howard, and E. K. H. Salje, Cubic calcite and its structural phase transitions, Phys. Chem. Miner. **52**, 7 (2025).

[9] D. J. Barber and H. R. Wenk, Deformation twinning in calcite, dolomite, and other rhombohedral carbonates, Phys. Chem. Miner. **5**, 141 (1979).

[10] H.-R. Wenk, D. J. Barber, and R. J. Reeder, Microstructures in carbonates, Rev. Mineral. Geochem. **11**, 301 (1983).

[11] S. Bueble and W. W. Schmahl, Mechanical twinning in calcite considered with the concept of ferroelasticity, Phys. Chem. Miner. **26**, 668 (1999).

[12] E. K. H. Salje, Multiferroic domain boundaries as active memory devices: Trajectories towards domain boundary engineering, ChemPhysChem **11**, 940 (2010).

[13] X. He, S. Li, X. Ding, J. Sun, S. M. Selbach, and E. K. H. Salje, The interaction between vacancies and twin walls, junctions, and kinks, and their mechanical properties in ferroelastic materials, Acta Mater. **178**, 26 (2019).

[14] D. H. Warner, S. J. Grutzik, and A. G. Ilgen, The dual effect of surface adsorbates on fracture of calcite, Scr. Mater. **242**, 115952 (2024).

[15] J. Lastam, E. Griesshaber, X. Yin, U. Rupp, I. Sanchez-Almazo, M. Heß, P. Walther, A. Checa, and W. W. Schmahl, The unique fibrilar to platy nano-and microstructure of twinned rotaliid foraminiferal shell calcite, Sci. Rep. **13**, 2189 (2023).

[16] X. Yin, E. Griesshaber, A. Checa, F. Nindiyasari-Behal, I. Sánchez-Almazo, A. Ziegler, and W. W. Schmahl, Calcite crystal orientation patterns in the bilayers of laminated shells of benthic rotaliid foraminifera, J. Struct. Biol. **213**, 107707 (2021).

[17] L. Li and C. Ortiz, Pervasive nanoscale deformation twinning as a catalyst for efficient energy dissipation in a bioceramic armour, Nat. Mater. **13**, 501 (2014).

[18] Z. Deng, L. Chen, and L. Li, Comparative nanoindentation study of biogenic and geological calcite, J. Mech. Behav. Biomed. Mater. **137**, 105538 (2023).

[19] L. Li, J. C. Weaver, and C. Ortiz, Hierarchical structural design for fracture resistance in the shell of the pteropod *Clio pyramidata*, Nat. Commun. **6**, 6216 (2015).

[20] L. Seybold, C. A. Trepmann, S. Hölzl, K. Pollok, F. Langenhorst, F. Dellefant, and M. Kaliwoda, Twinned calcite as an indicator of high differential stresses and low shock pressure conditions during impact cratering, Meteorit. Planet. Sci. **58**, 1287 (2023).

[21] A. S. Côté, R. Darkins, and D. M. Duffy, Deformation twinning and the role of amino acids and magnesium in calcite hardness from molecular simulation, Phys. Chem. Chem. Phys. **17**, 20178 (2015).

[22] Y. Yang, Y. Lin, X. Ding, J. Sun, N. J. Butterfield, J. Aufort, and E. K. H. Salje, $\{10\bar{1}4\}$ twin boundary in calcite: Structure and physical properties, Phys. Rev. B **110**, 144112 (2024).

[23] L. Yang, C. E. Killian, M. Kunz, N. Tamura, and P. Gilbert, Biomineral nanoparticles are space-filling, Nanoscale **3**, 603 (2011).

[24] J. D. Rodriguez-Blanco, S. Shaw, and L. G. Benning, The kinetics and mechanisms of amorphous calcium carbonate (ACC) crystallization to calcite, via vaterite, Nanoscale **3**, 265 (2011).

[25] A. Lázár *et al.*, Insights into the amorphous calcium carbonate (ACC) → ikaite → calcite transformations, CrystEngComm **25**, 738 (2023).

[26] L. Wang, X. Jiang, X. He, J. Chu, Y. Xiao, H. Liu, and E. K. H. Salje, Crackling noise and bio-cementation, Eng. Fract. Mech. **247**, 107675 (2021).

[27] S. Van Aert, S. Turner, R. Delville, D. Schryvers, G. Van Tendeloo, and E. K. H. Salje, Direct observation of ferrielectricity at ferroelastic domain boundaries in $CaTiO_3$ by electron microscopy, Adv. Mater. **24**, 523 (2012).

[28] J. Gonnissen, D. Batuk, G. F. Nataf, L. Jones, A. M. Abakumov, S. Van Aert, D. Schryvers, and E. K. H. Salje, Direct observation of ferroelectric domain walls in $LiNbO_3$: Wall-meanders, kinks, and local electric charges, Adv. Funct. Mater. **26**, 7599 (2016).

[29] L. Goncalves-Ferreira, S. A. T. Redfern, E. Artacho, E. Salje, and W. T. Lee, Trapping of oxygen vacancies in the twin walls of perovskite, Phys. Rev. B **81**, 024109 (2010).

[30] M. U. Rothmann, W. Li, Y. Zhu, U. Bach, L. Spiccia, J. Etheridge, and Y.-B. Cheng, Direct observation of intrinsic twin domains in tetragonal $CH_3NH_3PbI_3$, Nat. Commun. **8**, 14547 (2017).

[31] V. A. Oliveira *et al.*, Formation mechanism and properties of twinned structures in (111) seeded directionally solidified solar grade silicon, Acta Mater. **121**, 24 (2016).

[32] Y.-C. Wu, M.-F. Hung, and P.-W. Su, Improving the performance of nanowires polycrystalline silicon twin thin-film transistors nonvolatile memory by NH_3 plasma passivation, J. Electrochem. Soc. **158**, H578 (2011).

[33] A. Aird and E. K. H. Salje, Enhanced reactivity of domain walls in with sodium, Eur. Phys. J. B **15**, 205 (2000).

[34] A. Aird and E. K. H. Salje, Sheet superconductivity in twin walls: Experimental evidence of WO_3, J. Phys.: Condens. Matter **10**, L377 (1998).

[35] M. A. Carpenter and E. K. H. Salje, Elastic anomalies in minerals due to structural phase transitions, Eur. J. Mineral. **10**, 693 (1998).

[36] B. Houchmandzadeh, J. Lajzerowicz, and E. Salje, Order parameter coupling and chirality of domain walls, J. Phys.: Condens. Matter **3**, 5163 (1991).

[37] E. K. H. Salje, A. Graeme-Barber, M. A. Carpenter, and U. Bismayer, Lattice parameters, spontaneous strain and phase transitions in $Pb_3(PO_4)_2$, Acta Crystallogr. Sect. B: Struct. Sci. **49**, 387 (1993).

[38] S. Marais, V. Heine, C. Nex, and E. Salje, Phenomena due to strain coupling in phase transitions, Phys. Rev. Lett. **66**, 2480 (1991).

[39] B. Wruck, E. K. H. Salje, M. Zhang, T. Abraham, and U. Bismayer, On the thickness of ferroelastic twin walls in lead phosphate $Pb_3(PO_4)_2$ an x-ray diffraction study, Phase Transit. **48**, 135 (1994).

[40] U. Bismayer and E. Salje, Ferroelastic phases in $Pb_3(PO_4)_2$-$Pb_3(AsO_4)_2$; X-ray and optical experiments, Acta Cryst. **37**, 145 (1981).

[41] W. T. Lee, E. K. H. Salje, L. Goncalves-Ferreira, M. Daraktchiev, and U. Bismayer, Intrinsic activation energy for twin-wall motion in the ferroelastic perovskite $CaTiO_3$, Phys. Rev. B **73**, 214110 (2006).

[42] H. Yokota, H. Usami, R. Haumont, P. Hicher, J. Kaneshiro, E. K. H. Salje, and Y. Uesu, Direct evidence of polar nature of ferroelastic twin boundaries in $CaTiO_3$ obtained by second harmonic generation microscope, Phys. Rev. B **89**, 144109 (2014).

[43] H. Yokota, S. Matsumoto, E. K. H. Salje, and Y. Uesu, Polar nature of domain boundaries in purely ferroelastic $Pb_3(PO_4)_2$ investigated by second harmonic generation microscopy, Phys. Rev. B **100**, 024101 (2019).

[44] H. Yokota, S. Matsumoto, N. Hasegawa, E. K. H. Salje, and Y. Uesu, Enhancement of polar nature of domain boundaries in ferroelastic $Pb_3(PO_4)_2$ by doping divalent-metal ions, J. Phys.: Condens. Matter **32**, 345401 (2020).

[45] J. H. E. Cartwright, A. G. Checa, J. D. Gale, D. Gebauer, and C. I. Sainz-Díaz, Calcium carbonate polyamorphism and its role in biomineralization: How many amorphous calcium carbonates are there? Angew. Chem. Int. Ed. **51**, 11960 (2012).

[46] G. Lu, S. Li, X. Ding, J. Sun, and E. K. H. Salje, Electrically driven ferroelastic domain walls, domain wall interactions, and moving needle domains, Phys. Rev. Mater. **3**, 114405 (2019).

[47] S. Rios, E. K. H. Salje, M. Zhang, and R. C. Ewing, Amorphization in zircon: Evidence for direct impact damage, J. Phys.: Condens. Matter **12**, 2401 (2000).

[48] G. C. Capitani, H. Leroux, J. C. Doukhan, S. Ríos, M. Zhang, and E. K. H. Salje, A TEM investigation of natural metamict zircons: Structure and recovery of amorphous domains, Phys. Chem. Miner. **27**, 545 (2000).

[49] P. Németh, Diffraction features from $(10\bar{1}4)$ calcite twins mimicking crystallographic ordering, Minerals **11**, 720 (2021).

[50] M. Bruno, F. R. Massaro, M. Rubbo, M. Prencipe, and D. Aquilano, (10.4), (01.8), (01.2), and (00.1) twin laws of calcite ($CaCO_3$): Equilibrium geometry of the twin boundary interfaces and twinning energy, Cryst. Growth Des. **10**, 3102 (2010).

[51] P. Raiteri, R. Demichelis, and J. D. Gale, Thermodynamically consistent force field for molecular dynamics simulations of alkaline-earth carbonates and their aqueous speciation, J. Phys. Chem. C **119**, 24447 (2015).

[52] M. Parrinello and A. Rahman, Polymorphic transitions in single-crystals: a new molecular-dynamics method, J. Appl. Phys. **52**, 7182 (1981).

[53] S. Nosé, A unified formulation of the constant temperature molecular dynamics methods, J. Chem. Phys. **81**, 511 (1984).

[54] W. G. Hoover, Canonical dynamics: Equilibrium phase-space distributions, Phys. Rev. A **31**, 1695 (1985).

[55] S. Plimpton, Fast parallel algorithms for short-range molecular-dynamics, J. Comput. Phys. **117**, 1 (1995).

[56] A. Stukowski, Visualization and analysis of atomistic simulation data with OVITO—the open visualization tool, Modell. Simul. Mater. Sci. Eng. **18**, 015012 (2009).

[57] A. Stukowski and K. Albe, Dislocation detection algorithm for atomistic simulations, Modell. Simul. Mater. Sci. Eng. **18**, 025016 (2010).

[58] H. T. Stokes, S. van Orden, and B. J. Campbell, ISOSUBGROUP: An internet tool for generating isotropy subgroups of crystallographic space groups, J. Appl. Crystallogr. **49**, 1849 (2016).

[59] E. Salje, Phase transitions in ferroelastic and co-elastic crystals, Ferroelectrics **104**, 111 (1990).

[60] See Supplemental Material at http://link.aps.org/supplemental/10.1103/mpmg-71ck for mean value of the tilting angle in spherical distributed CO_3^{2-} anions, relevant closed-form equations for the linear-quadratic coupling of Q_T and Q_Γ, and a Schematic illustration of the orientation of CO_3^{2-} triangles in $R\bar{3}c$ calcite; agreement in the probability distribution functions at different temperatures indicates equivalence of spatial and temporal averaging of $Q_{\mathrm{T}i}$ and $Q_{\Gamma i}$ and thickness dependency of twin wall polarization.

[61] E. Salje and B. Wruck, Specific-heat measurements and critical exponents of the ferroelastic phase transition in $Pb_3(PO_4)_2$ and $Pb_3(P_{1-x}As_xO_4)_2$, Phys. Rev. B **28**, 6510 (1983).

[62] D. D. Viehland and E. K. H. Salje, Domain boundary-dominated systems: Adaptive structures and functional twin boundaries, Adv. Phys. **63**, 267 (2014).

[63] B. Houchmanzadeh, J. Lajzerowicz, and E. Salje, Interfaces and ripple states in ferroelastic crystals—a simple model, Phase Transit. **38**, 77 (1992).

[64] J. F. Scott, E. K. H. Salje, and M. A. Carpenter, Domain wall damping and elastic softening in $SrTiO_3$: Evidence for polar twin walls, Phys. Rev. Lett. **109**, 187601 (2012).

[65] E. K. H. Salje and J. F. Scott, Ferroelectric Bloch-line switching: A paradigm for memory devices? Appl. Phys. Lett. **105**, 252904 (2014).

[66] E. K. H. Salje, X. Wang, X. Ding, and J. F. Scott, Ultrafast switching in avalanche-driven ferroelectrics by supersonic kink movements, Adv. Funct. Mater. **27**, 1700367 (2017).

[67] S. Matsunuma, H. Kagi, K. Komatsu, K. Maruyama, and T. Yoshino, Doping incompatible elements into calcite through amorphous calcium carbonate, Cryst. Growth Des. **14**, 5344 (2014).

[68] T. C. Nicholas, A. E. Stones, A. Patel, F. M. Michel, R. J. Reeder, D. G. A. L. Aarts, V. L. Deringer, and A. L. Goodwin, Geometrically frustrated interactions drive structural complexity in amorphous calcium carbonate, Nat. Chem. **16**, 36 (2024).

[69] H. Liu, Z. Wen, Z. Liu, Y. Yang, H. Wang, X. Xia, J. Ye, and Y. Liu, Unlocking the potential of amorphous calcium carbonate: A star ascending in the realm of biomedical application, Acta Pharm. Sin. B **14**, 602 (2024).

[70] Y. Li, H. Zeng, and H. Zhang, Influence of impurity metal doping on calcite growth: A first-principles study, Appl. Surf. Sci. **637**, 157927 (2023).

[71] H. Tian, X.-Y. Kuang, A.-J. Mao, Y. Yang, H. Xiang, C. Xu, S. O. Sayedaghaee, J. Íñiguez, and L. Bellaiche, Novel type of ferroelectricity in brownmillerite structures: A first-principles study, Phys. Rev. Mater. **2**, 084402 (2018).

[72] E. K. H. Salje, Ferroelastic materials, Annu. Rev. Mater. Res. **42**, 265 (2012).

[73] E. K. H. Salje, B. Wruck, and H. Thomas, Order-parameter saturation and low-temperature extension of Landau theory, Z. Phys. B: Condens. Matter **82**, 399 (1991).

[74] E. K. H. Salje, S. A. Hayward, and W. T. Lee, Ferroelastic phase transitions: Structure and microstructure, Found. Crystallogr. **61**, 3 (2005).

[75] E. K. H. Salje and M. A. Carpenter, Linear–quadratic order parameter coupling and multiferroic phase transitions, J. Phys.: Condens. Matter **23**, 462202 (2011).

[76] H. E. Boeke, Die Schmelzerscheinungen und die umkehrbare Umwandlung des Calciumcarbonats, Neues Jahrb. Mineral **1**, 121 (1912).

[77] M. Burkhard, Calcite twins, their geometry, appearance and significance as stress-strain markers and indicators of tectonic regime: A review, J. Struct. Geol. **15**, 351 (1993).

[78] H. Cölfen and M. Antonietti, Mesocrystals: Inorganic superstructures made by highly parallel crystallization and controlled alignment, Angew. Chem. Int. Ed. **44**, 5576 (2005).

[79] Y. Kim, M. Alexe, and E. K. H. Salje, Nanoscale properties of thin twin walls and surface layers in piezoelectric WO_{3-x}, Appl. Phys. Lett. **96**, 032904 (2010).

[80] P. Maksymovych, J. Seidel, Y. H. Chu, P. Wu, A. P. Baddorf, L.-Q. Chen, S. V. Kalinin, and R. Ramesh, Dynamic conductivity of ferroelectric domain walls in $BiFeO_3$, Nano Lett. **11**, 1906 (2011).

[81] M. Schröder, A. Haußmann, A. Thiessen, E. Soergel, T. Woike, and L. M. Eng, Conducting domain walls in lithium niobate single crystals, Adv. Funct. Mater. **22**, 3936 (2012).

[82] L. Goncalves-Ferreira, S. A. T. Redfern, E. Artacho, and E. K. H. Salje, Ferrielectric twin walls in $CaTiO_3$, Phys. Rev. Lett. **101**, 097602 (2008).

[83] T. Zykova-Timan and E. K. H. Salje, Highly mobile vortex structures inside polar twin boundaries in $SrTiO_3$, Appl. Phys. Lett. **104**, 082907 (2014).

[84] E. Salje, B. Kuscholke, B. Wruck, and H. Kroll, Thermodynamics of sodium feldspar II: Experimental results and numerical calculations, Phys. Chem. Miner. **12**, 99 (1985).

[85] E. Salje, Thermodynamics of sodium feldspar I: Order parameter treatment and strain induced coupling effects, Phys. Chem. Miner. **12**, 93 (1985).

[86] S. Conti, S. Müller, A. Poliakovsky, and E. K. H. Salje, Coupling of order parameters, chirality, and interfacial structures in multiferroic materials, J. Phys.: Condens. Matter **23**, 142203 (2011).

[87] E. K. H. Salje, S. Li, M. Stengel, P. Gumbsch, and X. Ding, Flexoelectricity and the polarity of complex ferroelastic twin patterns, Phys. Rev. B **94**, 024114 (2016).

[88] H. Pöttker and E. K. H. Salje, Flexoelectricity, incommensurate phases and the Lifshitz point, J. Phys.: Condens. Matter **28**, 075902 (2016).

[89] G. Catalan *et al.*, Flexoelectric rotation of polarization in ferroelectric thin films, Nat. Mater. **10**, 963 (2011).

[90] G. Lu, X. Ding, J. Sun, and E. K. H. Salje, Wall-wall and kink-kink interactions in ferroelastic materials, Phys. Rev. B **106**, 144105 (2022).

[91] B. Baum and A. Spang, On the origin of the nucleus: A hypothesis, Microbiol. Mol. Biol. Rev. **87**, e00186 (2023).